

Improved Fixed Range Forgetting Factor-Adaptive Extended Kalman Filtering (FRFF-AEKF) Algorithm for the State of Charge Estimation of High-Power Lithium-Ion Batteries

Etse Dablu Bobobee, Shunli Wang^{}, Chuanyun Zou, Emmanuel Appiah, Heng Zhou,
Paul Takyi-Aninakwa, Md. Amdadul Haque*

School of Information Engineering, Southwest University of Science and Technology, Mianyang
621010, China

*E-mail: 497420789@qq.com

Received: 2 June 2022 / Accepted: 23 July 2022 / Published: 10 October 2022

The lithium-ion battery is perhaps the most powerful energy storage media available today and is used in virtually all electronic devices, especially electric and hybrid electric vehicles. The battery industry is growing rapidly in battery technology, development, and production to meet future demands. The difficulty in estimating battery states such as the state of charge (SOC) has led to the discovery of several methods and techniques. The use of improved algorithms coupled with a combination of methods and models has contributed immensely toward the accurate estimation of battery states. In this paper, the state of charge of the high-power lithium-ion battery is estimated based on an improved Fixed Range Forgetting Factor-Adaptive Extended Kalman filtering (FRFF-AEKF) algorithm. The interference of system noise is overcome with the use of the fixed range forgetting factor and the Saga-Husa adaptive filter (SHAF) to calculate the SOC more accurately. The experiments performed for the acquisition of data, parameterization, and verification of results, the methods employed and the use of the improved algorithm were all done to accurately estimate the SOC. Two other algorithms, the Adaptive extended Kalman filtering (AEKF) algorithm, and the Adaptive Unscented Kalman filtering (AUKF) algorithm are used as benchmarks for verifying the performance of the improved FRFF-AEKF algorithm. The improved FRFF-AEKF algorithm achieved 99.74 % estimation accuracy under Hybrid Pulse Power Characterization (HPPC) test working conditions and 99.44 % under Beijing Bus Dynamic stress test (BBDST) working conditions. The estimation accuracy of the AEKF algorithm under HPPC and BBDST conditions was 98.37% and 99.27% respectively, and the estimation accuracy of the AUKF algorithm under HPPC and BBDST conditions was 97.97% and 99.07% respectively. The verification experiment proved that the method was successful and can accurately estimate the state of charge of the high-power lithium-ion battery.

Keywords: Lithium-ion batteries; state of charge; Thevenin equivalent model; fixed range forgetting factor; adaptive extended Kalman filtering algorithm

1. INTRODUCTION

Evolution in the automobile industry is witnessing a shift towards electric and hybrid electric vehicles with a high dependency on lithium-ion batteries. Lithium-ion batteries are the most suitable energy storage for powering electric vehicles (EVs) due to the lack of memory effect, longer lifespan, higher energy, and higher power densities [1, 2]. The sharp growth in the electric vehicle market is attributed to the global increase in the cost of fuel, increased demand for fuel-efficient, high-performance, and low-emission vehicles, and reduction in the cost of electric vehicle batteries [3, 4]. Government policies and regulations on vehicle emissions towards reducing pollution and limiting climate change are also major factors [5, 6]. Many advanced battery management systems (BMSs) have been developed with a claim of high accuracy in the estimation of battery characteristic states. To obtain optimum results, good performance, and guarantee a longer lithium-ion battery lifespan, it is important to calibrate the parameters and battery states as accurately as possible to avoid damage [7, 8]. The lithium-ion battery is the most preferred battery used in portable electronic devices, and recently in power tools, transportation, electric grids, and electric/hybrid electric vehicles [9-11]. This is due to its several advantages over other battery technologies including environmental friendliness [12-14]. The state of charge is an important battery characteristic in power electronics and especially in EVs because it is the equivalence of a fuel gauge and needs to be determined to optimize the performance of the battery management system [15-17]. The appropriateness and complexity of the methods and techniques used for battery state estimation determine the approach, process, and accuracy of estimation.

Researchers have proposed several methods and techniques to estimate the SOC of lithium-ion batteries with a great focus on intelligent, improved, and adaptive algorithms, and battery models. These methods can be categorized as direct, model-based, and data-driven estimation methods [18, 19]. Direct methods include the coulomb counting or ampere-hour (Ah) integral method and the open-circuit voltage (OCV) method [20, 21]. The electrochemical models (EMs), the equivalent circuit models (ECMs), and the electrochemical impedance models (EIMs) are examples of Model-based methods [22, 23]. This method is based on the use of battery models and the identification of battery capacity, internal resistance, and other parameters. Additionally, state observers used by model-based techniques include the Kalman filter, the extended Kalman filter (EKF), the adaptive extended Kalman filter, the unscented Kalman filter (UKF), the sliding mode observer (SMO), the particle filter (PF), and the H-infinity observer [24-26]. Data-driven methods include k-nearest neighbor (k-NN) regression, fuzzy controller, the neural network, and the support vector machine [27, 28]. There are four types of lithium-ion battery models: fractional-order models (FOMs), equivalent circuit models, and electrochemical models (NNMs) [29]. Improved methods of SOC estimation allow for real-time estimation, reduction in system noise towards accurate estimation, and good error correction capabilities. Battery modeling, parameter identification, and SOC estimation are all important to improve estimation accuracy. During experimentation on the lithium-ion battery, it is important to note that it requires protection from over-charging and over-discharging, and needs special management to avoid the destruction of the battery [30]. Therefore, in estimating the SOC of the battery, the choice of an appropriate model is essential.

The UKF and EKF of the conventional Kalman algorithm regard system noise as white noise or observation noise, respectively. In doing so, the noise characteristics in real-world applications are

disregarded, which has an impact on the SOC estimation's precision [31]. For an accurate SOC estimation, the AEKF algorithm depends on the precise estimation of the battery's model capacity and parameters [32, 33]. In order to ensure the covariance matrix's non-negative definiteness for a multi-scale dual Kalman filter algorithm, square root decomposition was performed on it. The SHAF was then used to update the noise variable. A fixed-length error innovation sequence (EIS) of the AEKF technique was used to create an innovation covariance matrix (ICM) without taking the distribution change of the EIS into account [34]. The ICM was updated based on the subsequent EIS to increase the accuracy of the SOC estimation. An intelligent adaptive extended Kalman filter (IAEKF) was developed to detect the moment of distribution change of the EIS via the greatest likelihood function. A fading filter and linear-nonlinear filtering based on the conventional EKF were used to increase noise adaption, which led to the creation of an improved EKF algorithm [35]. The statistical properties of measurement noise were adaptively rectified using a forgetting factor in the IAEKF algorithm. When calculating the actual innovation covariance matrix, the Sage-Husa EKF (SHEKF) and error covariance matrix are adaptively corrected per the invention, adopting a variable sliding window length [36]. An improved AUKF algorithm and SHAF can suppress the non-positive definiteness of error [37]. By estimating and correcting the system noise statistics adaptively, the adaptive algorithms can increase the SOC estimation stability and accuracy. To improve the accuracy of SOC estimation under charge/discharge conditions, an adaptive forgetting factor regression least-squares-extended Kalman filter (AFFRLS-EKF) SOC estimation strategy was proposed by reconstructing the forgetting factor of the least squares algorithm [38]. The SOC estimation accuracy of the battery based on the ECM is improved by an adaptive forgetting factor least squares and an unscented Kalman filtering algorithm [39]. The forgetting factor is changed in real time according to the model demand using the simulated annealing optimization algorithm. The incorporation of a Sage-Husa noise estimator into the noise-adaptive-interacting multiple model-unscented Kalman filter (NA-IMM-UKF) allowed the entire UKF model set to estimate and correct noise information in real-time for posterior and unknown noise information to be adaptively adjusted [40]. To optimize the algorithm, a forgetting factor was also introduced, which solved the problem of slow convergence of the Sage-Husa noise estimator when used in conjunction with the UKF algorithm. Although adaptive Sage window methods such as innovation-based adaptive estimation (IAE) and residual-based adaptive estimation (RAE) are widely used in AKF algorithms, they have several drawbacks. To overcome these limitations, an improved AUKF based on forgetting-factor-weight smoothing and multi-factor adaptation was used [41].

For parameter identification, a Thevenin equivalent circuit model is established and the recursive least squares with forgetting factor (FFRLS) method is used [42]. An evaluation factor is defined, and fuzzy control is used to realize the mapping between the evaluation factor and the forgetting factor's correction value, as well as to realize the forgetting factor's adaptive adjustment, and a noise adaptive algorithm is introduced into the AEKF algorithm to estimate the SOC. The forgetting factor is intended to reduce the instantaneous error of the estimated parameters and improve system stability. Because the values are between 0 and 1, the higher the value, the stronger the system's anti-interference ability [38]. The usual range of forgetting factor is 0.95~1 and the experimental data reveals that identified parameters of the ECM are more accurate and converge faster when the range of forgetting factor is selected as 0.98~1 [43]. The forgetting factor can be changed adaptively with the identified error of parameters

given the range 0.98-1, thus the larger the error value, the smaller the forgetting factor. Challenges such as the selection of the forgetting factor, poor robustness, and vulnerability of the EKF and UKF algorithms to noise, make the use of the AEKF algorithm most appropriate for parameter identification and accurate SOC estimation [42]. A variable forgetting factor recursive least squares (VFFRLS) algorithm was used to identify parameters and update the forgetting factor based on the innovation sequence, and an adaptive tracking EKF (ATEKF) algorithm was developed to accurately estimate the battery's SOC [44]. For parameter identification, the VFFRLS and AEKF algorithms are combined in real-time, together with the UKF algorithm that calculates SOC in real-time [45]. The use of the forgetting factor is therefore efficient and more accurate if the variable range is smaller reducing errors in the estimation.

The equivalent circuit model is known to be the most commonly used battery model due to its high accuracy and simplicity [46]. A First-order Thevenin equivalent circuit containing an ohmic internal resistance, polarization resistance, and polarization capacitance is modeled, and data from the HPPC experiment is used for battery parameterization. An improved FRFF-AEKF algorithm is proposed for the accurate estimation of SOC through the elimination of noise interference with the implementation of the SHAF. The range of forgetting factors is fixed between a variable range of 0.997~1. This is to improve adaptability, reduce noise during the estimation and achieve faster convergence with reduced error and increase accuracy. To verify the effectiveness of the method for accurate SOC estimation, SOC estimation with the AEKF and AUKF algorithm is compared with the improved FRFF-AEKF algorithm under HPPC and BBDST conditions. The paper is organized into sections, where after the abstract, section 1 is the introduction, section 2, is the mathematical analysis, section 3, is the experimental analysis, and section 4, is the conclusion.

2. MATHEMATICAL ANALYSIS

2.1 Definition of state of charge

The lithium-ion battery's state of charge is expressed as the battery's remaining capacity and is calculated as the ratio of remaining capacity to maximum available capacity. The mathematical formula for the state of charge of the battery can therefore be expressed as shown in Eq. (1)

$$\begin{cases} S_t = \frac{C_t}{C_{MAX}} \times 100\% \\ S_t = S_0 - \frac{\int_{t_0}^t \eta I(t) \eta dt}{C_{MAX}} \end{cases} \quad (1)$$

Where S_t is the current estimated SOC, C_t is the remaining battery capacity, C_{MAX} is the maximum available capacity when the battery is fully charged, S_0 is the initial SOC when the estimation process starts, η denotes the Coulombic efficiency, and $I(t)$ is the load current.

2.2 Battery Equivalent Model Construction

The choice of a battery model is paramount for accurate parameterization towards reflecting the battery's dynamic and static characteristics. The First-order Thevenin equivalent model is established and used in this research due to its simplicity, ease of use, and practical application as was proposed and implemented in [47-49] for SOC estimation. The established First-order Thevenin circuit model is shown in Figure 1.

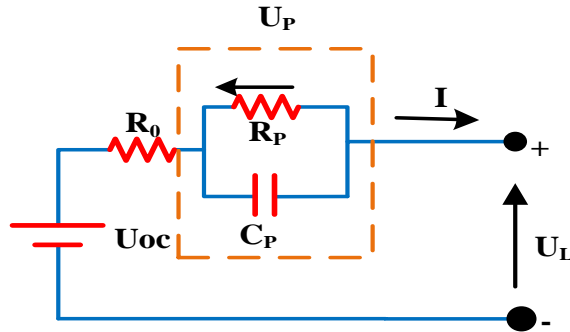


Figure 1. First-order Thevenin equivalent circuit model

Where U_{oc} is the open-circuit voltage, U_L is the load voltage, R_0 is the ohmic internal resistance, R_p represents the polarization resistance of the lithium-ion battery, C_p is the polarization capacitance, I indicates the load current, where the discharge direction is positive, and U_p indicates voltage across the RC. The circuit model in Figure 1 can be expressed mathematically as shown in Eq. (2).

$$\begin{cases} U_L = U_{oc} - IR_0 - U_p \\ \frac{dU_p}{dt} = \frac{I}{C_p} - \frac{U_p}{R_p C_p} \end{cases} \quad (2)$$

For the identification of battery parameters and estimation of SOC, the battery is considered as a nonlinear system with its dynamics represented in a state-space form. Using the definition of the state of charge, the battery's state-space equation can be expressed as shown in Eq. (3).

$$\begin{cases} X_k = \begin{bmatrix} S_k \\ U_{p,k} \end{bmatrix} = \begin{bmatrix} 1 & 0 \\ 0 & e^{-\frac{\Delta t}{\tau}} \end{bmatrix} \begin{bmatrix} S_k \\ U_{p,k} \end{bmatrix} + \begin{bmatrix} -\eta \frac{\Delta t}{C_{max}} \\ R_p (1 - e^{-\frac{\Delta t}{\tau}}) \end{bmatrix} I_k + w \\ U_{L,k} = U_{oc}(S_k) - U_{p,k} - I_k R_0 + v \end{cases} \quad (3)$$

Where $x_k = [S_k, U_{p,k}]^T$ is the state-space variable, $u_k = I_k$ is the input variable, and $y_k = U_{L,k}$ is the output variable, k represents the value of the corresponding variable at time step k , Δt is the sampling interval time, $\tau = R_p C_p$, w is the state error and v is the measurement error, representing zero-mean white noises of the covariance matrices Q and R , respectively.

2.3 Parameter identification

Through the HPPC test, experimental data is obtained and the voltage variations for charge and discharge are identified. Parameters of the First-order Thevenin equivalent model constructed as shown in Figure 1 are calculated, and the relationship between the SOC and OCV is established. A partially enlarged single voltage variation curve used for the identification of the parameters is shown in Figure 2.

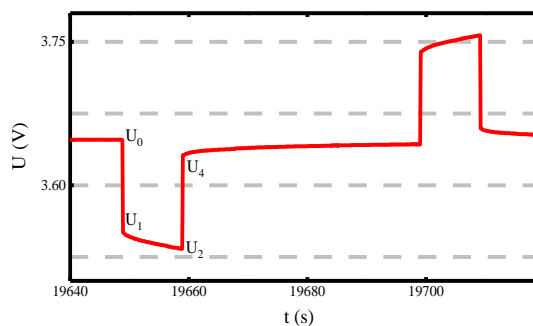


Figure 2. Partially enlarged single voltage variation curve

The voltage at which the battery remains stable at both the positive and negative terminals when the battery is left to rest for a prolonged period is known as the open-circuit voltage or U_{oc} . According to experiments, the voltage stabilizes and can be taken to be equal to the battery's OCV after the battery has had time to rest for 40 minutes. The battery model's calculation of U_L is consequently indicated in Eq.(4).

$$\begin{cases} U_L = U_{oc} - IR_p e^{-\frac{t}{\tau}} \\ U_L = U_{oc} - IR_0 - IR_p (1 - e^{-\frac{t}{\tau}}) \end{cases} \quad (4)$$

The parameters of the First-order equivalent circuit model are extracted based on the mathematical expressions and results from the calculations performed on the data acquired from the HPPC test. The identified parameters can be expressed as shown in Eq. (5)

$$\begin{cases} y = a - b(1 - e^{-\frac{x}{c}}) \\ a = U_{oc} - IR_0 \\ b = IR_p \\ c = R_p C_p \end{cases} \quad (5)$$

According to Figure 2, the corresponding parameters of the First-order Thevenin equivalent model, the ohmic internal resistance R_0 , the polarization resistance R_p , and polarization capacitance C_p can be calculated as shown in Eq. (6).

$$\begin{cases} R_0 = \frac{|U_1 - U_2| + |U_3 - U_4|}{2I_L} \\ R_p = \frac{b}{I} \\ C_p = \frac{c}{R_p} \end{cases} \quad (6)$$

The expression of the time constant is established to arrive at the specific times of the variation for accurate parameterization. Based on the time interval used in the HPPC experiment and the variation curve shown in Figure 2, the time constant is calculated as shown in Eq. (7).

$$\tau = - \frac{t_4 - t_3}{\ln\left(\frac{U_1 - U_4}{U_1 - U_3}\right)} \quad (7)$$

2.4 OCV/SOC relationship

The recorded voltages after each standby step are taken into consideration as the final open-circuit voltages in the HPPC test. All open-circuit voltage readings at various SOC are monitored and recorded. To determine the OCV/SOC relationship, the data is imported and used in the curve fitting. The change in OCV with SOC is displayed in Figure 3.

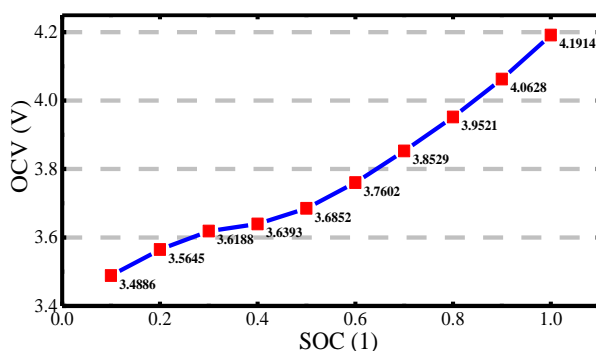


Figure 3. OCV/SOC relationship

The number of bends in the line is calculated, and one is added for the appropriate battery model order, to carry out further calculations, solve mathematically for the OCV, and establish the proper polynomial term to include. The polynomial curve reveals the mathematical expression shown in Eq. (8)

$$OCV = 34.7152 \times SOC^6 - 107.1463 \times SOC^5 + 123.054 \times SOC^4 - 63.4580 \times SOC^3 + 14.0830 \times SOC^2 - 0.5059 \times SOC + 3.4497 \quad (8)$$

A more accurate simulation data can be achieved when the parameter fitting polynomial corresponding to the curve is perfect. The polynomial function serves as input into the model in Simulink/MATLAB for updating subsystems in the simulation. The values of the variables *a*, *b*, and *c*,

according to equation 5 and the values of parameters extracted, identified, and calculated are presented in Table 1.

Table 1. Values of parameters at different SOC points.

SOC (%)	OCV (V)	a	b	c	R _o (Ω)	R _p (Ω)	C _p (F)
100	4.1914	4.104	0.02478	0.7888	0.002155	0.00062	1273.285
90	4.0628	3.976	0.02594	0.7832	0.00214	0.000649	1207.71
80	3.9521	3.863	0.02713	0.7787	0.002195	0.000678	1148.102
70	3.8529	3.761	0.02856	0.807	0.00228	0.000714	1130.252
60	3.7602	3.667	0.02857	0.7922	0.00231	0.000714	1109.135
50	3.6852	3.59	0.022	0.7764	0.002358	0.00055	1411.636
40	3.6393	3.549	0.02145	0.7776	0.002417	0.000536	1450.07
30	3.6188	3.517	0.02304	0.8234	0.002503	0.000576	1429.514
20	3.5645	3.458	0.02571	0.7853	0.002613	0.000643	1221.781
10	3.4886	3.372	0.03375	0.7023	0.002837	0.000844	832.3556

2.5 Iterative algorithm

2.5.1 The Improved Fixed Range Forgetting Factor-Adaptive Extended Kalman Algorithm

The state-space equation of the established First-order Thevenin equivalent circuit of the lithium-ion battery is expressed mathematically as shown in Eq. (9).

$$\begin{cases} x_{k+1} = f(x_k, u_k) + w_k \\ y_k = g(x_k, u_k) + v_k \end{cases} \tag{9}$$

The functions of $f(*)$ and $g(*)$ are nonlinear equations, where x_k is the n-dimensional system state vector at time point k , and w is the n-dimensional system noise vector. The function $f(x_k, u_k)$ is a non-linear state transition function. The second equation is the observation equation, where y is an observation vector, and v is a multi-dimensional system interference vector at time point k . The w_k and v_k are discretized to handle the process noise and to reduce noise with covariance matrices Q and R respectively. The function can be further explored to obtain Eq. (10).

$$\begin{cases} x_{k+1} = A_k x_k + B_k u_k + w_k \\ y_k = C_k x_k + D_k u_k + v_k \end{cases} \tag{10}$$

Where matrices A and C are the derivative matrices of the function (x, u) and $g(x, u)$ to the state vector respectively. Matrices B and D are the derivative matrices of the system input of the two functions respectively. The matrices $A, B, C,$ and D are represented as shown in Eq. (11).

$$\begin{cases} A_k = \frac{\partial(x_k, u_k)}{\partial x_k} = \begin{pmatrix} 1 & 0 \\ 0 & 1 - \frac{\Delta t}{C_p R_p} \end{pmatrix} \\ B_k = \frac{\partial(x_k, u_k)}{\partial x_k} = \begin{pmatrix} -\frac{\Delta t}{C_n} \\ \frac{\Delta t}{C_p} \end{pmatrix} \\ C_k = \frac{\partial(x_k, u_k)}{\partial u_k} = \left(\frac{\partial OCV}{\partial SOC} - 1 \right) \\ D_k = \frac{\partial(x_k, u_k)}{\partial u_k} = (-R_o) \end{cases} \quad (11)$$

The algorithm's estimation process includes time and measurement updates. The prediction process is another name for the time update process which predicts the current state variable in a single step and provides a prior estimation process for the next moment. The process of providing feedback observations and correcting deviations is referred to as the measurement update process. The improved FRRF-AEKF algorithm works as follows.

- (1). The initial condition of the filter for $k=0$ is set as shown in Eq. (12). Where x_0 represents the initial state value and P_0 represents the initial covariance.

$$x_0 = E(x), P_0 = \text{Var}(x) \quad (12)$$

- (2). The state vector estimates the time update of the algorithm is as shown in Eq. (13). Where $x_{k|k-1}$ is the state variable predicted at time k and x_{k-1} is the corrected state variable.

$$x_{k|k-1} = f(x_{k-1}, u_{k-1}) \quad (13)$$

- (3). The state covariance time update is as shown in Eq. (14).

$$P_{k|k-1} = F P_{k-1} F^T + Q_k \quad (14)$$

- (4). The Kalman-gain coefficient is calculated as shown in Eq. (15).

$$K_k = P_{k|k-1} H^T (H P_{k|k-1} H^T + R_k)^{-1} \quad (15)$$

- (5). The state vector measurement update of the algorithm is as shown in Eq. (16).

$$x_k = x_{k|k-1} + K_k (y_k - h(x_{k|k-1}, u_k)) \quad (16)$$

- (6). The state covariance matrix is updated as shown in Eq. (17).

$$P_k = (I - K_k H) P_{k|k-1} \quad (17)$$

Based on the equations listed for the improved FRRF-AEKF algorithm, $x_{k|k-1}$ is the direct time estimate at time k , and x_{k-1} is the optimal estimate state value at the last moment. P_k is the covariance update of x_k , Q_k is the covariance of process noise w , K_k is the Kalman-gain coefficient and R_k is the covariance of the observation noise v .

Because the covariance matrix, P_k , is decomposed, it is assured that P_k is always a non-negative definite, which can overcome the filter divergence caused by the computer's limited word length. The Sage-Husa filter adaptively updates the four noise variables and allows for accurate state estimation by

comparing the final estimated value to the estimated value. The process of calculating estimator-related quantities is shown in Eq. (18).

$$\begin{cases} \tilde{y}_k = y_k - h(x_k, u_k) - R_{k-1} \\ Q_k = \frac{1}{k} \sum_{i=0}^{k-1} (K_k \tilde{y}_k \tilde{y}_k^T K_k^T + P_k - FP_{k/k-1} F^T) \\ R_k = \frac{1}{k} \sum_{i=0}^{k-1} (\tilde{y}_k \tilde{y}_k^T - HP_{k/k-1} H^T) \end{cases} \quad (18)$$

This paper considers noise at both the previous and current moments at the same time to reduce noise, improve accuracy, and avoid the influence of the observed value on the estimated value and adopts the weighting coefficients $d_k = (1-b)/(1-b^{k+1})$, where b represents the fixed forgetting factor ranging $0.997 \leq b \leq 1$. This is a sequence with values in the fixed range which is implemented to introduce a temporal adaptivity in the estimation. The fixed range of forgetting factors improves the estimation accuracy and converges quickly as the value is randomly selected from the small fixed range given to reduce error in estimation. The fixed range forgetting factor is implemented as shown in Eq. (19).

$$\begin{cases} Q_k = (1-d_{k-1})Q_{k-1} + d_{k-1} (K_k \tilde{y}_k \tilde{y}_k^T K_k^T + P_k - FP_{k/k-1} F^T) \\ R_k = (1-d_{k-1})R_{k-1} + d_{k-1} (\tilde{y}_k \tilde{y}_k^T - HP_{k/k-1} H^T) \end{cases} \quad (19)$$

The process noise and observation noise are corrected to obtain better accuracy, the improved FRFF-AEKF algorithm process is computed as a loop starting from the initialization equation in Eq. (12) to Eq. (19) and data is collected during the process for accurate estimation of SOC. The complete process of the proposed improvement to the algorithm is shown in Figure 4.

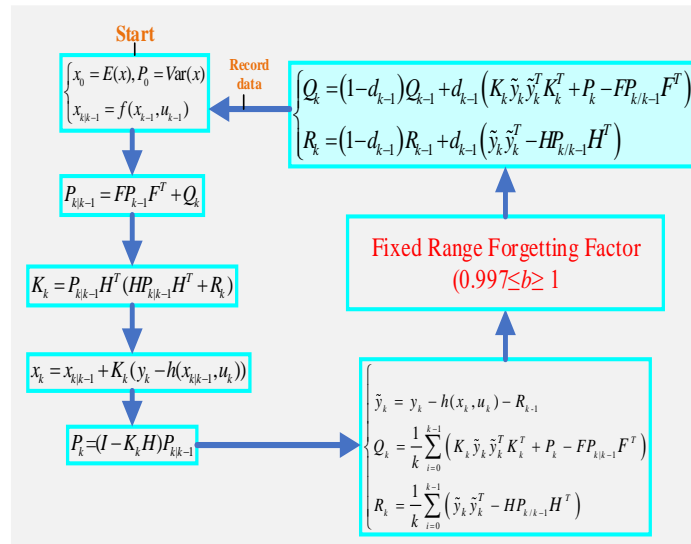


Figure 4. The improved FRFF-AEKF algorithm process

The adaptability and effectiveness of the fixed range forgetting factor towards improved accuracy of SOC estimation for the FRFF-AEKF algorithm is the random selection of the best factor in the given

range in real-time for faster convergence. The algorithm is verified based on the parameterized values of the First-order equivalent model and compared with the estimation accuracy of the AEKF and AUKF algorithms.

3. EXPERIMENTAL ANALYSIS

3.1 Test platform construction

The 3.7 V, 50 Ah high-power lithium-ion battery chosen as the test object for this experiment has a charge cut-off voltage of 4.2 V and a discharge cut-off voltage of 2.75 V. The BTS 750-200-100-4 test equipment has a maximum charge/discharge power of 750 W, a maximum voltage of 200 V, and a maximum current of 100 A. The fundamental properties of the lithium-ion battery are illustrated in Table 2.

Table 2. Basic technical parameters of the battery

Factor	Specification
Size: length * width * height/ mm	148×27×92
Rated voltage/V	3.7
Maximum load current /A	5C
Rated capacity/Ah	50
Charge cut-off voltage/V	4.2
Discharge cutoff voltage/V	2.75

The connection of the battery to the test machine, which is also connected to a computer, is required for the experiment setup with a specific terminal chosen from among the 16 available terminals. The computer's software is then programmed to follow a logical algorithm to complete the task. The experimental setup of the various components is shown in Figure 5.

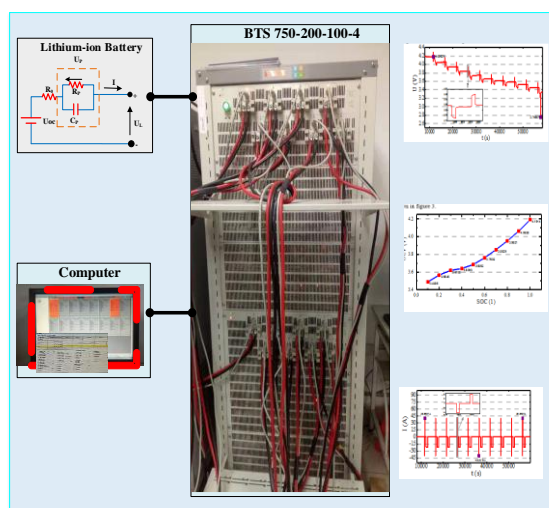


Figure 5. Experimental Setup

3.2 Capacity and Hybrid Pulse Power Characterization Test

The Capacity and HPPC tests are used to identify the parameters of the established First-order Thevenin equivalent model and to calculate the parameters required for SOC estimation. A single HPPC working step was performed, consisting of a 1C (current 50 A) constant current charge 10s, shelve for 40 s, and 1C (current 50 A) constant current charge 10s, followed by shelving [50-52]. During parameter identification, the functional relationships of resistance, capacitance, voltage, and SOC were determined. The battery was modeled in Simulink/MATLAB to create a First-order Thevenin equivalent circuit that mimicked the actual battery characteristics. The improved FRFF-AEKF algorithm was incorporated into the model and the parameters identified from the HPPC experimental data are subsequently used in the estimation of the SOC.

3.3 Results, verification, and comparison

3.3.1 Capacity test result

The capacity experiment was carried out to calibrate the battery's capacity, energy, current, and voltage. These various parameters can be deduced from the capacity experiment and compared with the information provided by the manufacturer to determine whether the experiment was successful or not. The results of the capacity test are shown in Figure 6.

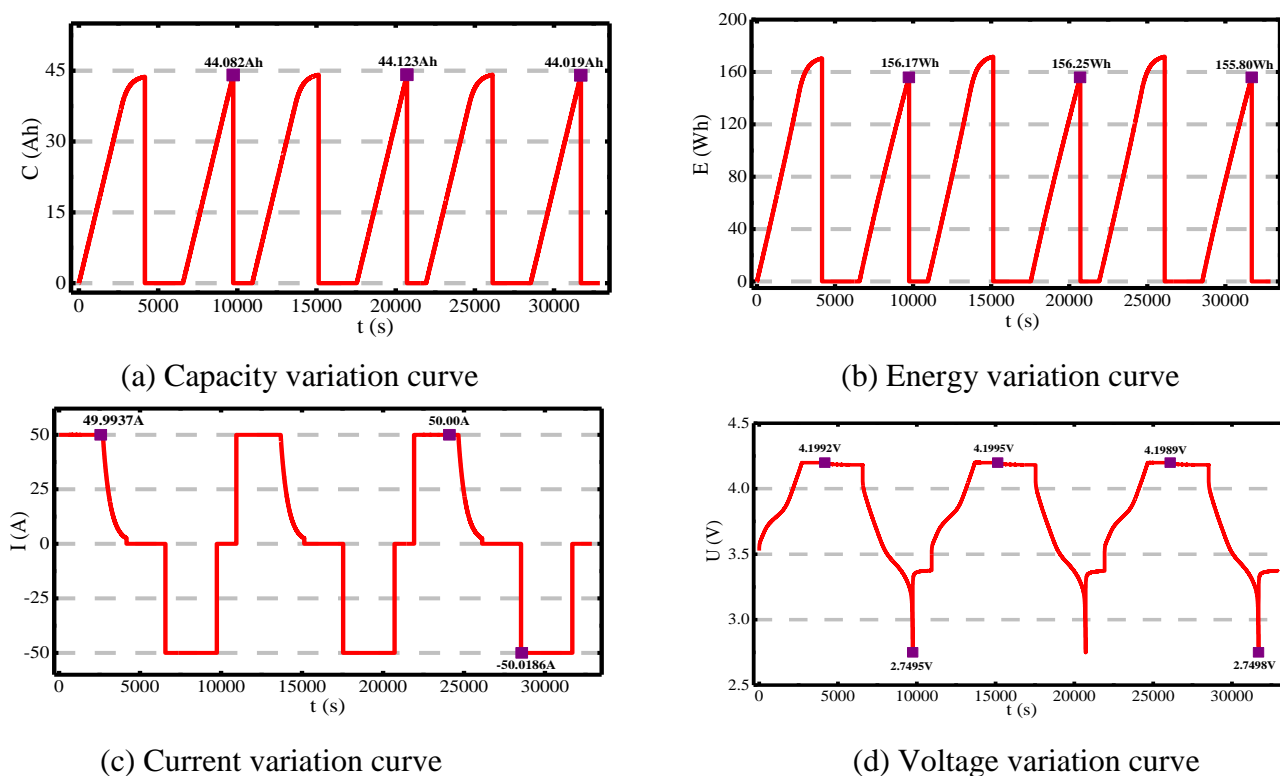


Figure 6. Capacity test results

Figure 6 (a) is the capacity variation curve with time showing the battery's capacity as approximately 50Ah. The experiment yielded three maximum values: 44.082 Ah, 44.123 Ah, and 44.019 Ah.

Figure 6 (b) shows the energy variation curve and the three maximum energy values obtained in the experiment are 156.17 Wh, 156.25 Wh, and 155.80 Wh. As a result, the battery's energy is approximately 160Wh.

Figure 6 (c) depicts the current variation and the maximum and minimum current values obtained in the experiment, which are 50.0 A and -50.0186 A, respectively.

Figure 6 (d) is the voltage variation curve and the maximum and minimum values obtained in the experiment as 4.1995 V, which is approximately the maximum voltage of the battery stated as 4.2 V, and 2.7495 V, which is approximately the minimum voltage of the battery stated earlier as 2.75 V.

The current and voltage flow can be seen and analyzed as shown in Figure 7.

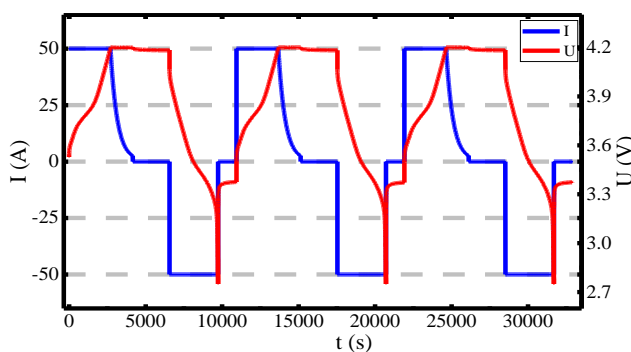
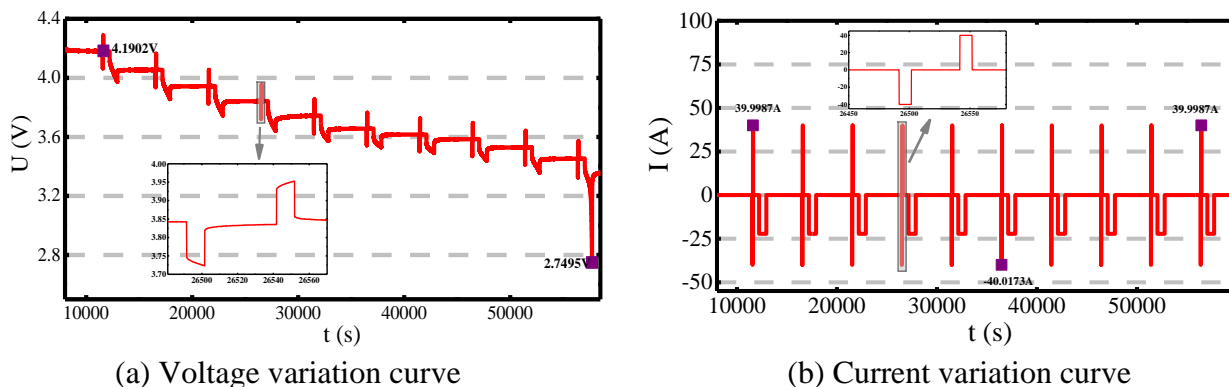


Figure 7. Voltage/Current discharge variation curve

In Figure 7 , the variation curves of the current and voltage from the capacity test are compared to illustrate the capacity of the battery.

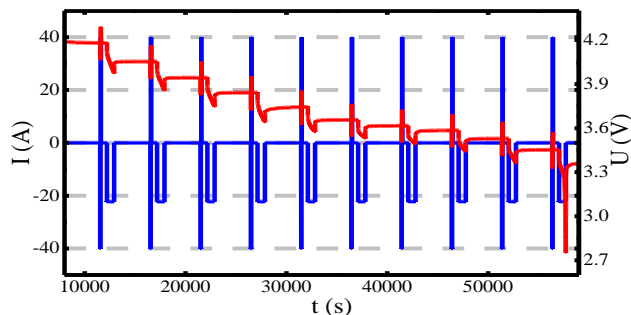
3.3.2 HPPC test results

The HPPC test result was used to identify each OCV at a specific SOC point and for battery parameterization. The voltage and current time variation curves are shown in Figure 8.



(a) Voltage variation curve

(b) Current variation curve



(c) Voltage/Current discharge variation curve

Figure 8. HPPC test result

In Figure 8 (a) and (b), the voltage and current variation curves show that the battery terminal voltage decreases as the number of cycles increases and the current variation shows that as the number of cycles increases, so does the discharge current.

Figure 8 (c) compares the voltage and current variation curves from the HPPC experiment over time. The figure's overlaying curves depict the actual occurrence of the battery at specific times.

3.4 SOC estimation result

SOC estimation was then based on the experimental results and parameterization. The estimation shows a downward slope with time as SOC decreases from 1 to 0.1 as shown in Figure 9.

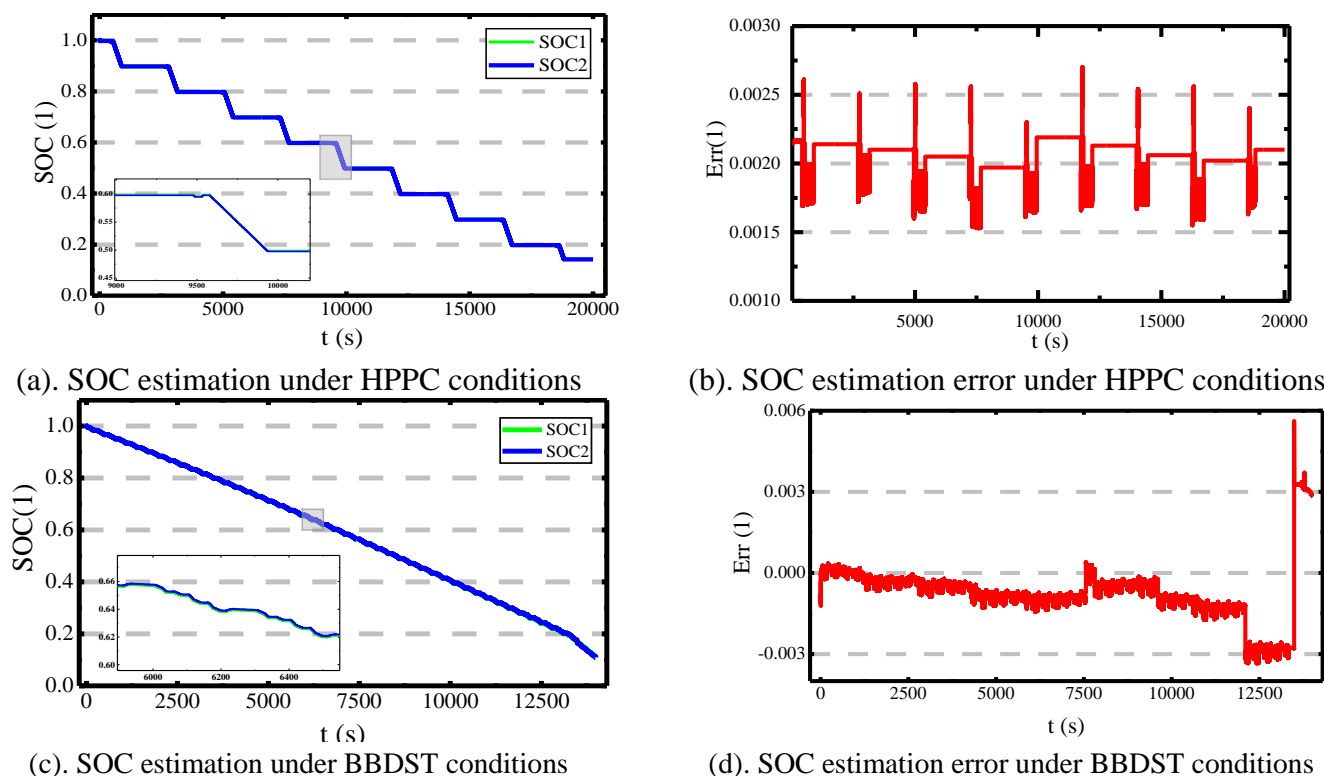


Figure 9. SOC estimation variation curves

It can be observed from Figure 9 that there is a gradual decrease and fluctuating trend due to the alternating charge and discharge during the experiment, with the discharge time being longer than the charging time. Figure 9 (a) represents the SOC estimation variation curve under HPPC conditions and Figure 9 (b), the error of estimation. SOC1 represents the true SOC, while SOC2 represents the SOC estimation based on the improved FRFF-AEKF algorithm. Figure 9 (c) depicts the SOC estimation variation curve under BBDST conditions, and Figure 9 (d), the estimation error. SOC1 represents the true SOC, while SOC2 represents the SOC estimation based on the improved FRFF-AEKF algorithm. The proposed improved FRFF-AEKF algorithm achieved a maximum estimation error of 0.26% under HPPC working conditions and 0.56% under BBDST conditions. This result is better than the outcome achieved in [42, 43, 53], which used similar algorithms for soc estimation.

3.5 Verification of results

3.5.1 Voltage characteristics

The simulation results were compared to the HPPC test results to confirm the validity of the SOC estimated values.

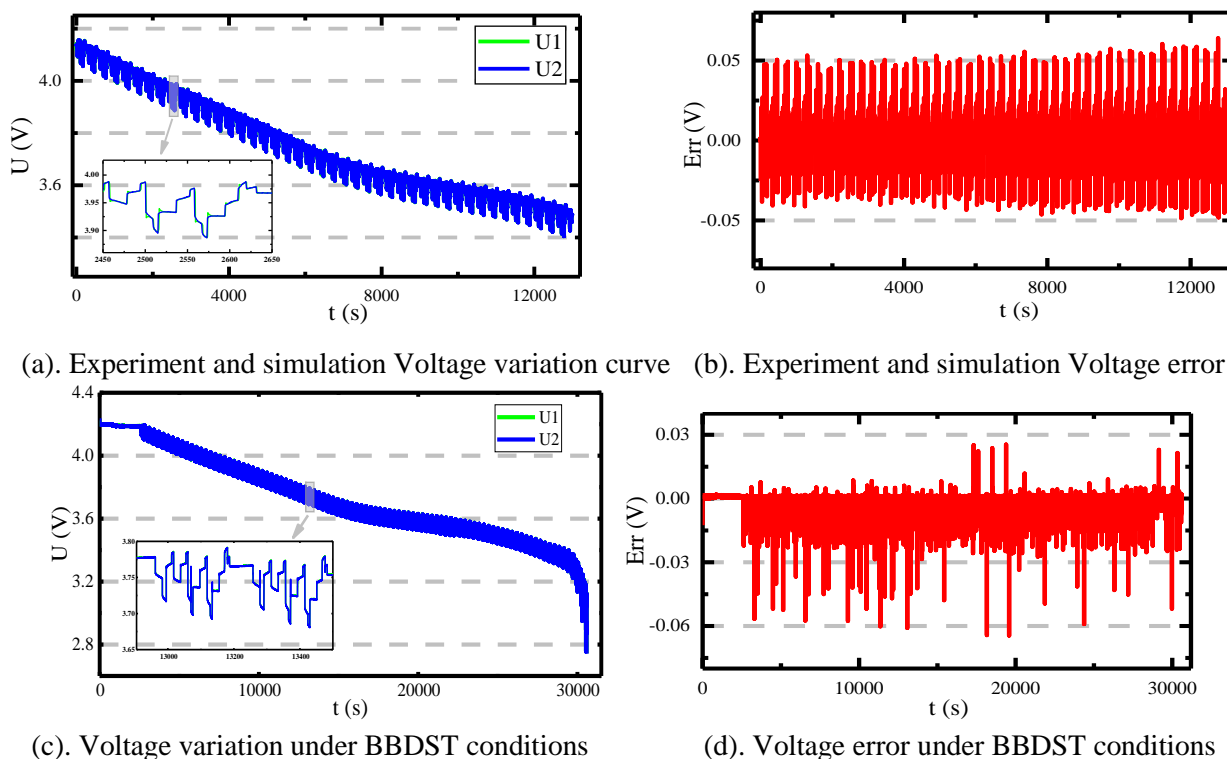


Figure 10. Comparison of voltage variation curves

The simulation terminal voltage is obtained by using the simulation model and the value of the current (I) in the experimental data is obtained by the test equipment. The Beijing Bus Dynamic Stress Test (BBDST) working condition experiment was designed and carried out to demonstrate the

adaptability and performance of the improved FRFF-AEKF algorithm and to validate the algorithm's effectiveness for accurate SOC. The experiment was carried out under the complex operating conditions of the lithium-ion battery to thoroughly test the practicability and robustness of the algorithms. Results from the simulation and the BBDST experiment are compared to the experimental terminal voltage variation curve as shown in Figure 10

The voltage variation and voltage error curves as shown in Figure 10 (a) and (b), respectively. Where U1 represents the change curve of the real terminal voltage data collected through the HPPC test, whereas U2 represents the output terminal voltage curve generated in the simulation model.

The voltage variation and voltage error curves are shown in Figure 10 (a) and (b), respectively. Where U1 represents the change curve of the real terminal voltage data collected through the HPPC test, whereas U2 represents the output terminal voltage curve generated in the simulation model. The figure displays the overall variation trend across all simulation and experiment curves as well as how closely the curves resemble the actual test curve. As a result, the findings can be confirmed as valid for use in any calculation leading to an accurate estimation of SOC.

3.5.2 Comparison and Verification of SOC estimation result

To evaluate and confirm the accuracy and effective operation of the model and proposed algorithm, SOC estimation results from the proposed established model and the application of the improved FRFF-AEKF method are compared. The comparison between the SOC and error estimate variation curves is illustrated in Figure 11.

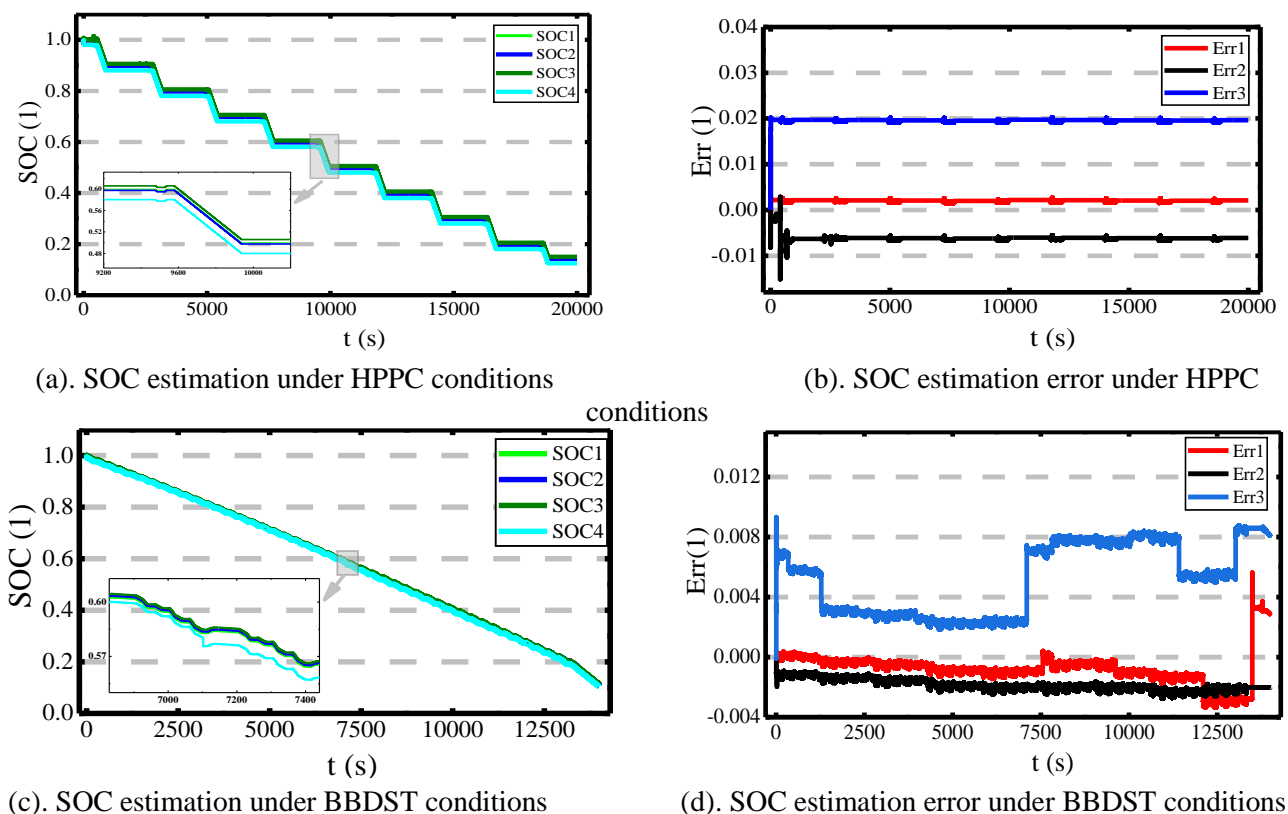


Figure 11. Comparison of SOC estimation verification variation curves

Figure 11 (a) is the SOC estimation variation curve under HPPC conditions, where SOC1 is the true SOC, SOC2 is the SOC estimation based on the improved FRFF-AEKF algorithm, and SOC3 and SOC4 are SOC estimations based on the AEKF and AUKF algorithms respectively. Figure 11 (b) is the estimation error curve, where Err1 is the estimation error curve based on the FRFF-AEKF algorithm, and Err2 and Err3 are SOC estimation error curves based on the AEKF and AUKF algorithms respectively.

Figure 11 (c) is the SOC estimation variation curve under BBDST conditions, where SOC1 is the true SOC, SOC2 is the SOC estimation based on the FRFF-AEKF, and SOC3 and SOC4 are SOC estimations based on the AEKF and AUKF algorithms respectively. Figure 11 (d) is the estimation error curve, where Err1 is the estimation error curve based on the FRFF-AEKF algorithm, and Err2 and Err3 are SOC estimation error curves based on the AEKF and AUKF algorithms respectively.

Comparing the results of the proposed algorithm to similar algorithms implemented in [34, 35, 42] for SOC estimation, the improved FRFF-AEKF algorithm converges faster and has a better accuracy of 99.74% under HPPC working conditions and 99.44% under BBDST working conditions. The estimation accuracy of the AEKF algorithm under HPPC conditions was 98.37% and 99.27% under BBDST conditions. While the estimation accuracy of the AUKF algorithm under HPPC and BBDST conditions was 97.97% and 99.07% respectively.

4. CONCLUSIONS

To accurately estimate SOC, data from the HPPC test for parameterization is obtained in this study and employed in a number of simulations with an enhanced Fixed Range Forgetting Factor-Adaptive extended Kalman filtering technique. The Saga-Husa adaptive filter is used to reduce system noise and improve the accuracy of estimation. The test conditions for data gathering, model parameterization, simulation, and verification of results for comparison were HPPC and BBDST. When the results from the HPPC working condition were compared to the results from the BBDST working condition, it was determined that the proposed approach performed better both in terms of algorithm and method. The performance of the improved algorithm was verified using two other algorithms, the Adaptive extended Kalman filter, and the Adaptive Unscented Kalman filter. The results show that the proposed improved FRFF-AEKF algorithm performed marginally better than the other two algorithms with a maximum estimation error of 0.26% under HPPC working conditions and 0.56% under BBDST working conditions as compared to a maximum estimation error of 1.63% and 0.73% for the AEKF algorithm under HPPC and BBDST working conditions respectively. The maximum estimation error of the AUKF algorithm under HPPC and BBDST working conditions was 2.03% and 0.93% respectively. The accuracy of SOC estimation based on the improved algorithm is verified by this outcome. The result also shows that the algorithm can quickly converge to realize accurate SOC estimation of lithium-ion batteries and offer critical data for application in electronic vehicles, smart grids, and other applications including electronic devices for quality and reliable evaluation. Further work on this paper will involve improving the algorithm's performance and implementing it with high-order models such as the 2RC

and 3RC to look for any shift in variation that may indicate an external or internal influence on the model's change toward accurate SOC estimation.

ACKNOWLEDGMENTS

The work was supported by the National Natural Science Foundation of China (No. 62173281), and China Scholarship Council (No. 201908515099)

References

1. Y. Ding, Z.P. Cano, A. Yu, J. Lu, Z. Chen, *Electrochemical Energy Reviews*, 2 (2019) 1-28.
2. G. Zhao, X. Wang, M. Negnevitsky, *iScience*, 25 (2022) 103744.
3. A.K. Balaji, P.K. Soori, *Sustainable Transportation Infrastructure for Smart Cities in the Gulf Cooperation Council: The Case of Electric Vehicle Charging*, Springer Singapore, (2019), 107-121.
4. S. McDonagh, D.M. Wall, P. Deane, J.D. Murphy, *Renewable Energy*, 131 (2019) 364-371.
5. A. Srivastav, *Reducing Carbon Growth*, Springer Singapore, (2019), 111-146.
6. J. Kim, J. Oh, H. Lee, *Applied Thermal Engineering*, 149 (2019) 192-212.
7. Z. Wang, S. Zeng, J. Guo, T. Qin, *Energy*, 167 (2019) 661-669.
8. N. Noura, L. Boulon, S. Jemeï, *World Electric Vehicle Journal*, 11 (2020) 66.
9. L. Wang, D. Lu, Q. Liu, L. Liu, X. Zhao, *Electrochimica Acta*, 296 (2019) 1009-1017.
10. Q. Wang, L. Jiang, Y. Yu, J. Sun, *Nano Energy*, 55 (2019) 93-114.
11. Y. Fan, X. Chen, D. Legut, Q. Zhang, *Energy Storage Materials*, 16 (2019) 169-193.
12. J. Xiao, B. Niu, Q. Song, L. Zhan, Z. Xu, *Journal of Hazardous Materials*, 404 (2021) 123947.
13. Y.E. Durmus, H. Zhang, F. Baakes, G. Desmaizieres, H. Hayun, L. Yang, M. Kolek, V. Küpers, J. Janek, D. Mandler, *Advanced energy materials*, 10 (2020) 2000089.
14. Y. Bai, N. Muralidharan, Y.-K. Sun, S. Passerini, M.S. Whittingham, I. Belharouak, *Materials Today*, 41 (2020) 304-315.
15. J. Van Mierlo, M. Berecibar, M. El Baghdadi, C. De Cauwer, M. Messagie, T. Coosemans, V.A. Jacobs, O. Hegazy, *World Electric Vehicle Journal*, 12 (2021) 20.
16. B. Balasingam, M. Ahmed, K. Pattipati, *Energies*, 13 (2020) 2825.
17. Y. Wang, Z. Sun, Z. Chen, *Energy*, 175 (2019) 1055-1066.
18. R. Xiong, J. Cao, Q. Yu, H. He, F. Sun, *IEEE Access*, 6 (2018) 1832-1843.
19. H. Pan, Z. Lü, W. Lin, J. Li, L. Chen, *Energy*, 138 (2017) 764-775.
20. C. Limandibrata, *Determining the State of Charge and the State of Health of a Battery Pack*, University of Twente, (2021), 1-8.
21. X. Xiong, S.L. Wang, C. Fernandez, C.M. Yu, C.Y. Zou, C. Jiang, *International journal of energy research*, 44 (2020) 11385-11404.
22. R. Arun Chendhuran, J. Senthil Kumar, *Advances in Automation, Signal Processing, Instrumentation, and Control*, (2021) 2619-2625.
23. Q. Zhang, D. Wang, B. Yang, H. Dong, C. Zhu, Z. Hao, *Journal of Energy Storage*, 50 (2022) 104182.
24. W. Xu, J. Xu, X. Yan, *Journal of Power Electronics*, 20 (2020) 292-307.
25. C. Xu, E. Zhang, S. Yan, K. Jiang, K. Wang, Z. Wang, S. Cheng, *Journal of Energy Storage*, 45 (2022) 103701.
26. Y. Wang, J. Tian, Z. Sun, L. Wang, R. Xu, M. Li, Z. Chen, *Renewable and Sustainable Energy Reviews*, 131 (2020) 110015.
27. M.S.H. Lipu, M.A. Hannan, A. Hussain, M.M. Hoque, P.J. Ker, M.H.M. Saad, A. Ayob, *Journal of Cleaner Production*, 205 (2018) 115-133.
28. Z. Wang, X. Li, Y. Wang, *Journal of Physics: Conference Series*, 2109 (2021) 012005.

29. N. Li, Y. Zhang, F. He, L. Zhu, X. Zhang, Y. Ma, S. Wang, *Global Energy Interconnection*, 4 (2021) 619-630.
30. G. Jin, L. Li, Y. Xu, M. Hu, C. Fu, D. Qin, *Energies*, 13 (2020) 1785.
31. C. Jiang, S. Wang, B. Wu, C. Fernandez, X. Xiong, J. Coffie-Ken, *Energy*, 219 (2021) 119603.
32. P. Xu, J. Li, C. Sun, G. Yang, F. Sun, *Electronics*, 10 (2021) 122.
33. Z. Wang, G. Feng, D. Zhen, F. Gu, A. Ball, *Energy Reports*, 7 (2021) 5141-5161.
34. D. Sun, X. Yu, C. Wang, C. Zhang, R. Huang, Q. Zhou, T. Amietszajew, R. Bhagat, *Energy*, 214 (2021) 119025.
35. S. Yang, S. Zhou, Y. Hua, X. Zhou, X. Liu, Y. Pan, H. Ling, B. Wu, *Scientific reports*, 11 (2021) 1-15.
36. Z. Zhang, L. Jiang, L. Zhang, C. Huang, *Journal of Energy Storage*, 37 (2021) 102457.
37. J. Xing, P. Wu, *Sustainability*, 13 (2021) 5046.
38. M. Li, Y. Zhang, Z. Hu, Y. Zhang, J. Zhang, *Sensors (Basel)*, 21 (2021) 5698.
39. H. Wang, Y. Zheng, Y. Yu, *Mathematics*, 9 (2021) 1733.
40. C. Huang, X. Yu, Y. Wang, Y. Zhou, R. Li, *Energy Reports*, 7 (2021) 8152-8161.
41. J. Sun, L. Tao, Z. Niu, B. Zhu, *IEEE Access*, 8 (2020) 95321-95332.
42. N. Shi, Z. Chen, M. Niu, Z. He, Y. Wang, J. Cui, *Journal of Energy Storage*, 45 (2022) 103518.
43. X. Sun, J. Ji, B. Ren, C. Xie, D. Yan, *Energies*, 12 (2019) 2242.
44. D. Ma, K. Gao, Y. Mu, Z. Wei, R. Du, *Energies*, 15 (2022) 3499.
45. T. Ouyang, P. Xu, J. Chen, J. Lu, N. Chen, *Electrochimica Acta*, 353 (2020) 136576.
46. R. Xiong, J. Huang, Y. Duan, W. Shen, *Applied Energy*, 314 (2022) 118915.
47. L. Wang, Y. Xu, E. Wang, X. Zhao, S. Qiao, G. Li, H. Sun, *Journal of Energy Storage*, 51 (2022) 104565.
48. L. Ling, D. Sun, X. Yu, R. Huang, *Journal of Energy Storage*, 43 (2021) 103070.
49. S. Boulmrharj, R. Ouladsine, Y. NaitMalek, M. Bakhouya, K. Zine-dine, M. Khaidar, M. Siniti, *Journal of Energy Storage*, 30 (2020) 101518.
50. X. Xin, S.-L. Wang, C.-M. Yu, J. Cong, J. Coffie-Ken, *Int. J. Electrochem. Sci*, 15 (2020) 2226
51. M.-K. Tran, A. Mevawala, S. Panchal, K. Raahemifar, M. Fowler, R. Fraser, *Journal of Energy Storage*, 32 (2020) 101785.
52. L. Zhang, S. Wang, D.-I. Stroe, C. Zou, C. Fernandez, C. Yu, *Energies*, 13 (2020) 2057.
53. T. Xiao, X. Shi, B. Zhou, X. Wang, *Comparative Study of EKF and UKF for SOC Estimation of Lithium-ion Batteries*, *IEEE Access*, (2019) 1570-1575.